Accepted Manuscript
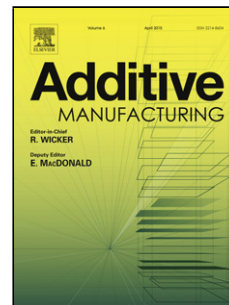
Title: Powder bed binder jetting additive manufacturing of silicone structures

Authors: Farzad Liravi, Mihaela Vlasea

Please cite this article as: { https://doi.org/

This is a PDF file of an unedited manuscript that has been accepted for publication. As a service to our customers we are providing this early version of the manuscript. The manuscript will undergo copyediting, typesetting, and review of the resulting proof before it is published in its final form. Please note that during the production process errors may be discovered which could affect the content, and all legal disclaimers that apply to the journal pertain.

Powder Bed Binder Jetting Additive Manufacturing of Silicone Structures

Farzad Liravi, Mihaela Vlasea

University of Waterloo, Department of Mechanical and Mechatronics Engineering, Waterloo, Ontario, N2L 3G1

Contact Author: Mihaela Vlasea, PhD

Address: Department of Mechanical and Mechatronics Engineering, University of Waterloo, Waterloo, Ontario, N2L 3G1 Canada, e-mail: mihaela.vlasea@uwaterloo.ca

1

Graphical Abstract:
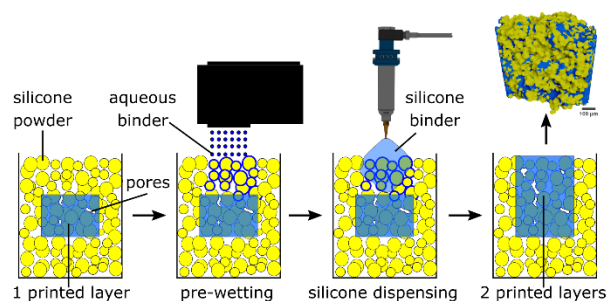
Powder bed binder jetting additive manufacturing was used for the first time to produce porous silicone (polysiloxane) structures.

Abstract:

The feasibility of a hybrid additive manufacturing (AM) method combining material extrusion and powder bed binder jetting (PBBJ) techniques for fabrication of structures made of silicone (polysiloxane) is investigated in this paper. A full factorial experimental design was conducted to maximize the geometrical accuracy of the parts. The rheological and morphological properties of the silicone powders, the thermal characteristics of the liquid silicone binder, and mechanical characterization the additively manufactured parts are reported. Using this hybrid AM method, porous cylindrical structures (5 mm diameter (D) × 3 mm height (H)) with potential applications in biomedical industry were additively manufactured. The final structures are composed of ~ 60% silicone powder, ~ 30% silicone binder, and <10% air voids. These three phases are distributed throughout the structure in a non-uniform fashion.

Key words:

2

1   Introduction

There has been an increased interest in manufacturing of complex-shaped silicone (polysiloxane) structures stemming from the commercialization of silicone in 1940's. This material has enabled revolutionary changes in different branches of the biomedical industry including the production of prostheses [1], phantoms [2], biosensors [3,4], and drug delivery systems [5]. The wide adoption of this family of polymers in fabrication of bio-structures has roots in its unique properties such as thermal resistance at high and low temperatures, weatherability, high gas permeability, low surface energy, and proven biocompatibility [6].

Over the past half a century, a combination of molding and manual refinement has been the unrivaled method for production of silicone objects. This method, however, is time-consuming and expensive, and requires long patient consultations as the products are highly custom, with intricate three-dimensional (3D) features. Moreover, manual methods are largely dependent on the skills of the clinicians or technicians executing the work [7]. Additive manufacturing (AM) approaches convert complex digital CAD models into layer-by-layer manufacturing execution steps to realize the part. AM approaches present opportunities for replacement of casting-based silicone manufacturing techniques, as AM enables high complexity in design and flexibility in production of custom parts without the need for specialized tooling or molds. Moreover, the layer-by-layer AM process allows for embedding of smart structures such as sensors, functionally-graded materials or design features during fabrication. This enables a new generation of smart silicone objects such as artificial muscles possible [8,9].

3D printing of molds was one of the first methods for improving silicone manufacturing process via AM techniques [10]. At the time, the deployment of AM significantly decreased the part variability by reducing the influence of the clinician on the final product, but the effect on

3

reducing the total production time and cost proved to be limited. Moreover, by employing silicone molding, the final product will be a passive object, with homogeneous internal properties or features. Other research groups have focused on the AM production of a part precursor from various structural biomaterials other than silicone such as the commercial acrylate-based Tango Plus (Stratasys, Minnesota, USA) and starch, followed by infiltration or coating with silicone at a later stage with methods such as dipping or wrapping [11-13]. These methods were not successful due to the faster physical degradation of the structural core material compared to silicone, however, the capability of AM in production of geometrically accurate structures with unprecedented level of details revealed the benefits of direct AM of silicone [14-16].

There are significant challenges associated with the AM of silicone. The largest obstacle is the high viscosity of the family of silicones available on the market that would result in structures with sufficient mechanical properties for biomedical applications (5.5 – 8 N/mm2 for tensile strength, 5 – 17 N/mm for tear strength, 500 – 1200% for elongation at break, 16 – 25 IRHD for hardness). Even though factors such as additives, fillers, and curing condition affect the mechanical properties of crosslinked polymers, it is generally understood that longer polymer chains, which result in higher viscosity, are the key to resilient polymers. Except for pneumatic extrusion and piezo-pneumatic jetting, current AM material dispensing methods are not able to handle highly viscous materials through refined nozzles at high resolution. Moreover, silicones are thermoset polymers, hence, their irreversible polymerization process makes them unfit for well-established polymer 3D printing techniques such as fused deposition modeling (FDM) or selective laser sintering (SLS).

Research and commercial efforts in AM of silicone materials have focused on material extrusion, vat photopolymerization or stereolithography (SLA), and material jetting, with various

degrees of success and technology-specific limitations. Of these AM methods, most of the research in the area of silicone AM has been focused on material extrusion [17-23]. In material extrusion, applying pressure using a mechanical or pneumatic system provides enough force to dispense a continuous flow of materials with up to 6×10^7 mPa.s viscosity [24,25]. The material extrusion system in the work of Duoss et al. (2014) is able to print silicone features with high quality in terms of the surface waviness, uniformity, and geometrical accuracy with a resolution as high as 100 μm and a maximum dispensing velocity of 20 mm/s [18]. Material extrusion of silicone inside a vat of viscoplastic material that acts as a support structure has made this process more reliable [26,27]. The first commercial silicone 3D printer (PICSIMA, Fripp Design and Research, UK) has been developed based on this approach [28]. Other efforts in the area of AM of silicone have focused on vat photopolymerization using SLA systems [7,29,30]. In stereolithography, the creation of a uniform layer is obtainable with resins of 300 – 5000 mPa.s viscosity [31,32]. Given the high viscosity of medical-grade silicones, in the SLA systems proposed for silicone, the part production happens in a static environment in the middle of the vat instead of the liquid-air interaction zone, eliminating the need for generating flow of silicone to the process zone. This new approach has a poor performance, with a 2 mm resolution resulting in a high degree of discrepancy between the 3D printed structures and their CAD models. Although there are technology gaps in terms of performance, using this approach, there is a good opportunity of employing mask-projection SLA instead of vector-scanning beams to enable a high speed AM technique for silicone. Aerosol jetting has also been used for printing 30 μm layers of silicone which is the highest vertical resolution achieved for this polymer [33]. Aerosol jetting, however, is a sluggish process with maximum 5 mm/s printhead speed. This technique is also only compatible with low viscous fluids. Generally, in regular inkjet printheads, depending on the jetting mechanism or

5

nozzle size, a maximum viscosity of $10 - 100$ mPa.s assures a successful droplet creation [24,32,34]. In author's previous work, a hybrid piezoelectric-pneumatic system was introduced that provided a reliable method for rapid (100 mm/s) fabrication of viscous (40,000 mPa.s at 10 s^{-1}) silicone polymers demonstrating a highly shear-thinning behavior [35].

To authors' best knowledge, powder bed binder jetting (PBBJ), also known as three-dimensional (3D) printing [36], has not been used prior for the fabrication of silicone structures. This method relies on AM of parts by converting a CAD model into layer-by-layer images that are sequentially printed onto thin layers of powder. The printed liquid acts as a binder, consolidating the powder into a so-called green part once the binder is cured. The thin layers of powder are spread using a counter-rotating roller or a blade mechanism from a douser or a feed bed. The green part is porous and typically undergoes a series of post-processing protocols, which may involve de-powdering, thermal treatments, or matrix infiltration. The materials used for PBBJ AM are mainly ceramics, metals, or their composites [34]. In a recent review of AM materials, PBBJ methods had not been introduced as a manufacturing method for any kind of thermoset polymer including silicone [37].

The PBBJ AM technique has shown great compatibility with bio-materials for multiple applications [38-43]. There are three main advantages for PBBJ manufacturing approaches: (1) the ability to use a wide range of materials [34,44-47], (2) the degree of freedom in manufacturing complex and scalable parts without the need for support structures [34,48], and (3) the high production speed with commercial systems performing often in the order of a few seconds per layer. In addition, PBBJ systems are capable of producing functionally graded structures [45,49-52], with multi-material or multi-colour features [11,53]. The versatility of this methodology is the driving factor in exploring PBBJ in manufacturing silicone structures. The most pressing

6

drawbacks in manufacturing silicone parts via PBBJ is that the smallest feature size of conventional PBBJ equipment is limited by the size distribution of the powder [44,54,55], by the binder jetting dispenser resolution [44], and de-powdering constraints [44,49,55,56]. For PBBJ, the minimum cavity feature size is typically considered at 500 μm for de-powdering considerations, with a layer thickness in the order of 25-200 μm. The powders used in PBBJ should comply with specific rheology and powder size distribution criteria to ensure uniform and defect-free layer properties in this layer thickness range. In addition, commercial PBBJ systems employ a single powder type during the build. The liquid binder is typically dispensed through a thermal or piezo printhead, with a general limit in viscosity of approximately 50-60 mPa.s to ensure proper material jetting, as well as fast infiltration through the powder substrate. The parts are typically exposed to a post-processing protocol for de-powdering, followed by heat-annealing, chemical setting, irradiation or infiltration, depending on the material system used. These post-processing steps typically result in part shrinkage or swelling and reduce the overall geometrical accuracy of the final product. The dimensional deviation can be considered in the CAD design stage by applying dimensional compensation factors.

To overcome some of the limitations in PBBJ, a new hybrid PBBJ and micro-deposition system was developed [48,57] to target manufacturing of functionally-graded parts with multi-material and custom variable porous structures. This new system employs multiple powder feed mechanisms to dynamically select and deploy up to three different powder compositions to each layer, thermal and piezo printhead delivery systems for jetting of various liquid binders, a variable counter-rotating roller mechanism to control powder compaction, a solid material dispenser for embedding discrete pore-generating sacrificial materials (porogens), and a micro-dispensing head

7

for deposition of liquids throughout the porous matrix of the part at select locations. A view of this system is shown in Figure 1.

In this study, the hybrid PBBJ AM system is used for the direct production of silicone structures. The system employs a material system composed of silicone powder as the base material in the substrate, a water-based liquid binder that is jetted through a thermal printhead onto the powder substrate to develop the wetted layer outline of the parts, and a thermoset silicone liquid binder to impart the necessary structural integrity of each layer. The thermoset silicone binder is heat cured after printing a fixed number of layers. Curing the thermoset silicone prevents any further permeation of subsequent silicone binder through previous layers, thus preserving the dimensions of the parts. The machine and material system is used to manufacture cylindrical shapes as part of a design of experiments (DoE). The results of this work are intended to lay the ground for hybrid PBBJ manufacturing of complex-shaped silicone parts as part of a forthcoming study.

2   Materials and Methods

2.1   Material System used in Additive Manufacturing of Parts

2.1.1   *Powder Silicone Materials*

Two hybrid organopolysiloxane powders consisting of spherical silicone rubbers were used as received in this research. These powder samples offer all of the unique properties of a regular polydimethylsiloxane (PDMS) rubber including high thermal resistance, weatherability, and biocompatibility. The first powder (powder A) consists of silicone rubbers covered with a silicone resin (KMP-602, Shin-Etsu Chemical, Tokyo, Japan). The resin cover provides high resistance to impact by relaxing the stress, and improves the lubricity property. The rubber part is responsible for the resistance to extreme temperatures and abrasion. The second silicone powder (powder B)

8

is made of pure spherical silicone rubbers without the resin coating (KMP-598, Shin-Etsu Chemical, Tokyo, Japan).

2.1.2 Liquid Silicone Binder Material

The two-part thermal-curable liquid silicone rubber (JY-9010, Changzhou Juyou New Material Tech Co., China) was used with 100:1 ratio of main precursor component to curing agent weight ratio. This silicone liquid is comprised of modified silica and Octamethylcyclotetrasiloxane which is a non-toxic organosilicon compound. The optimum precursor to curing agent ratio was selected based on the required crosslinking behavior of silicone inks to avoid clogging of the dispensing nozzle. A higher ratio of curing agent has proven to clog the nozzle, with a thermal curing response behavior as illustrated in Data in Brief, Figure 2.

2.1.3 Liquid Water-based Binder Material

An aqueous liquid binder (Zb®60, 3D systems, SC, USA) was inkjet printed onto the powder-bed to form the wetted precursor image of each layer. The Zb®60 includes 85-95% v/v of distilled water and 5-15% v/v of humectant and a proprietary polymer as a binding agent.

2.2 Additive Manufacturing of Parts

As the proof-of-concept, cylindrical structures (5 mm D × 3 mm H) were printed using the hybrid PBBJ AM system. The manufacturing steps are shown in Figure 2.. The process of manufacturing the silicone structures starts with designing cylindrical CAD models and slicing the digital data into successive layers and execution steps for each layer. The hybrid PBBJ AM of a 3D object with both the structural powder material and the binder made from silicone has four stages as illustrated in Figure 2. and described in detail as follows:

9

(1) A roller with a linear velocity of 20 mm/s and rotational velocity of 100 rpm spreads the silicone powder from a feeding bed (also called supply powder bed) to a build bed. This results in a flat layer of silicone powder with a fixed thickness (LT) (Figure 2.a).

(2) The thermal inkjet printhead jets the water-based Zb®60 binder onto the powder surface based on the image corresponding to the layer being manufactured. The Zb®60 liquid binder acts as a glue spread onto the silicone powder substrate to generate the structure by binding the silicone particles according to the geometry of the slice and to wet the substrate in preparation for the liquid silicone binder. Steps (1) and (2) are repeated a fixed number of times called dispensing frequency (Fr) before the deposition of liquid silicone is carried out (Figure.2.b) in step (3).

(3) The nozzle with inner diameter 100 μm is located above the center of the structure with 2 mm off-set. By applying 100 KPa air pressure through a micro-syringe extrusion system (Optimeter^{TM}, Nordson EFD, RI, USA), a droplet of silicone is dispensed to infiltrate the binder-wetted porous media substrate (Figure 2.c).

(4) The structure is then exposed to a temperature of $100 - 120$ °C supplied via a thermal lamp for 1 min to initiate and complete the polymerization of the two-part heat-curable silicone binder solution (Figure 2.d).

The four steps are repeated until the cylindrical structure is completed in a layer-by-layer fashion. The parts are left in the build bed for 2-3 hours. Finally, they are removed from the hybrid PBBJ system and air-heated at 85 °C to ensure the full curing.

2.3   Liquid Silicone Viscosity

The viscosity of liquid silicone binder was measured at 25 ± 0.01°C using a digital cone and plate rheometer (RST-CPS-P, Brookfield Engineering, MA, USA) at 200-2000 s^{-1} shear rate range by first increasing and then decreasing the shear rate value. The measurement data was collected at 15 points in 60 s for both ascendant and descendant curves.

2.4   Liquid Silicone Binder Differential Scanning Calorimetry (DSC)

The analysis of the thermal behaviour of liquid silicone binder was conducted using a DSC device (STA 449 F1, Netzsch, Germany) in the range of $25 - 160$ °C with a heating rate of 5 °C/min. In order to measure the curing time, the isothermal test was carried out with a DSC device (MTDSC 2920, TA Instruments, DE, USA) at the equilibrium temperatures of 90 °C, 100 °C, and 110 °C. The curing behaviour was investigated in an inert atmosphere (Nitrogen), and each test was replicated three times.

2.5   Silicone Powder Size and Morphology

The particle size distribution of the silicone powder samples and their sphericity and symmetry were verified using a dynamic image processing system (CamSizer XT, Retsch-Technology, Germany). The shadow of dispersed silicone particles illuminated by two LED sources were captured as they passed through a free-fall feed shaft in front of two CCD cameras. The system measured parameters corresponding to the particle size distribution, sphericity, and symmetry in real time.

2.6 Silicone Powder Dynamic Flowability, Shear Rate Sensitivity, and Bulk Properties

A powder rheometer (FT4, Freeman Technology, UK) was used to determine the rheological properties of the silicone powders in response to multiple external conditions such as flow rate, aeration, and consolidation, its bulk properties such as compressibility and permeability, and its shear rate sensitivity. Before conducting each test, a uniform initial state of stress was achieved at the conditioning stage by disturbing the particles gently through the helical movement of a blade.

2.7 Imaging

The liquid silicone binder droplet size at multiple pressure values were measured using a digital camera (AM7915MZT, Dino Lite, Taiwan) at 21× magnification. Images of the silicone binder droplets pendant from the needle tip were captured at 1 s intervals between the moment the pressure was applied, up to the separation of the droplet. The maximum diameter of droplet before separation was measured using the image processing software DinoCapture (Dino Lite, Taiwan). The powder silicone particle morphology was investigated using a scanning electron microscopy (SEM) (Ultra Plus, Carl Zeiss AG, Germany) at accelerating voltages of 10 kV and 3 kV for powder A and B, respectively.

2.8 Part 3D Profilometry

Three-dimensional (3D) profiles of the additively manufactured samples were obtained using a laser confocal microscope (VK-X250, Keyence, Japan) at 100× magnification. The height and the diameter of the circles fitted to the cross-section of the cylindrical samples were measured using the software MultiFileAnalyzer (Keyence, Japan).

2.9 Part Computed Tomography (CT) Scan

The tomography of the entire printed structure was captured using a nano-Computed Tomography (CT) scanner (Xradia 520 Versa, Carl Zeiss AG, Germany). The scanning parameters are provided in Table 1.

In order to calculate the solid phase density for 4.05 μm resolution CT scan result, the original greyscale image was filtered with both a small kernel Gaussian filter, then with a larger kernel bilateral filter (2 voxel radius) which is an edge preserving Gaussian filter. A greyscale threshold was then determined manually to segment the dense particle phase from the void and silicone binder phases. The exterior regions were masked from the part, to not be included in the porosity calculations. The masking was performed by eroding the surface down by a localized porosity threshold until the mask closely tracked the part surface. Then, each voxel within the masked region was given a distance value from the central axis, and another distance value from the base of the domain. These distance values were used to group voxels into radial and vertical position bins for the respective porosity distributions.

For separating three different phases of silicone powder, silicone binder, and air voids in the nano-scale CT scan results, the original greyscale image was first adjusted with a normalizing gradient to correct for artifacts associated with the sample exceeding the scanning field of view. A bilateral filter with a spatial radius of 2 voxel lengths was then applied to remove noise. Finally, the three phases were separated from each other in a combination of manual greyscale threshold selection and morphological image processing steps, including opening, closing, and three

13

dimensional median filters. The image processing routine had to be carefully performed due to the large overlap in the histograms of the porous and polymer phases.

2.10   Hardness

A Shore 00 handheld durometer (Shore S1, Shore Instruments-Instron, MA, USA) was used to measure the hardness of 3D printed samples as well as samples of the silicone binder cured in a mold for comparison. The rigid ball was located on the center of the cylindrical samples, and the hardness value was captured after 1s dwell time. Each reading was repeated three times for two replicates of samples manufactured under similar printing conditions.

2.11   Statistical Analysis

In order to optimize the 3D printing parameters, a multi-level experimental design was formed with the layer thickness (LT) and the dispensing frequency (Fr) of the silicone binder as the control factors. Table 2.shows the levels of each factor. The height (H), inner diameter (ID), and the diameter difference (DD) between the inner and outer circles fitted to the cross section of parts. The outer diameter (OD) is the diameter of the largest circle fitted to the cross-section of the cylindrical parts so that it covers the entire cross-section including the irregular edges. The diameter of the circle that only covers the central parts of the cross-section and not the irregularity caused by the lateral infiltration of silicone binder is ID. The difference between ID and OD is depicted in Figure 3. and is the method used to calculate DD.

The path to the optimized region for each parameter was found using the response surface method. Finally, all three responses were optimized simultaneously using desirability function technique (utility transfer function). The levels of significant factors were selected so that DD was minimized, and H and ID approached the target values of 3 mm and 5 mm, respectively.

14

A one-way Tukey Analysis of variance (ANOVA) at 95% confidence level was employed to compare the hardness of parts manufactured under different 3D printing conditions.

3   Results

3.1   Silicone Binder Viscosity and Droplet Size in Dispensing

Figure 4.a shows the viscosity of the silicone binder at the shear rate range of $200 - 2000$ s^{-1}. The viscosity vs. shear rate plot shows a Newtonian behavior with the constant viscosity of 78 mPa.s at room temperature. The ascendant and descendant plots coincide as well showing the independency of the rheological behavior of the fluid on the shearing history. For a fluid with the shown viscous behavior, the syringe dispensing was tested under various pressures. It was found that varying the dispensing air back-pressure did not affect the volume of the dispensed droplet, however, it changed the separation time (see Table 3). With a pressure of approximately 100 KPa, the droplet separated 8 seconds after the pressure was applied providing enough time for the control of dispensing mechanism. Figure 4.b shows the image of a silicone droplet captured before its separation form the needle tip with the inner diameter of 100 μm. The diameter of the shown droplet is 1.54 mm.

3.2   Thermal Analysis of Silicone Binder

The exothermic silicone cross-linking process for the samples of silicone binder at various hold temperatures are depicted in Figure 5.a. For all three replications of the experiment, the positive peak appears in the range of $75 - 90$ ºC. Thus, the maximum temperature of three tests (90 ºC) was selected for further investigation. The isothermal DSC results (Figure 5.b) at 90 ºC show that the curing process is accelerated after $3 - 4$ min at equilibrium and takes approximately 2 min to

reach the maximum curing rate. Similar experiment conducted at 100 ºC (Figure 5.c) shows that the curing happens right after the temperature equilibrium is reached. Increasing the temperature even further results in curing of the binder before reaching the target temperature (Figure 5.d). Increasing the amount of curing agent does not reduce the crosslinking speed significantly; however, it reduced the temperature at which the crosslinking initiates. The isothermal DSC results for a silicone binder with higher content of curing agent (100:2) at 85 – 100 ºC are shown in Figure 2 of Data in Brief. The results show a reduction in immediate initiation of crosslinking to 85 – 90 ºC which will increase the possibility of nozzle clogging. As a result, 100:1 mixing ratio was selected for this two-part silicone binder.

3.3 Silicone Powder Size and Morphology

The SEM images of powder A (Figure 6.a-c) and powder B (Figure 6..d-f) show their effective spherical morphology. The particles of powder A appear segregated, while the particles of powder B have cohered together and produced large agglomeration of clusters surrounded by finer satellite particles. The powder particles in both powder A and B appear spherical in nature. Powder A had a fine coating in the as-purchased state, and this can be seen as surface flakes in Figure 6.c. Powder B did not have any coating in the as-purchased state, and appears smooth in nature, as seen in Figure 6.f.

The particle size distribution of powder A can be seen in Figure 7.with an average particle size of 30 µm. The shape analysis test for powder A showed a high level of sphericity (average value of 0.842 for four test replications where 1 represents the perfect circle). The symmetry index for the powder A was 0.963 as well (with 1 representing the full symmetricity). Studying the particle size distribution and quantifying the sphericity of powder B was not possible due to its

16

high degree of agglomeration and cohesiveness. However, the manufacturer reports particle size distribution of 2 – 30 µm with an average particle size of 13 µm for this powder.

3.4 Silicone Powder Rheology

The flow properties of silicone powders were measured based on their resistance to the movement of a blade which creates a flow pattern by its rotational and vertical movement. Guidelines provided at [58-60] have been used to interpret the powder rheology results. The energy required to establish this flow pattern for both powders is shown in Figure 8.a. The first 8 repeated tests have been conducted at the same blade velocity, followed by the gradual decrease in the velocity in tests 9 – 12. At the fixed velocity region, the energy required for the flow is 15 mJ higher for the powder B. The same pattern with lower difference in the value of energy can be observed for the lower velocities. The lower energy for the powder A shows that it is a non-cohesive powder with better flow properties. This conclusion will be reaffirmed through other tests conducted.

A similar test was conducted for both powder types while they were conditioned with the air flow with varying velocities. The aeration test for powder A (Figure 8.b) and powder B (Figure 8.c) demonstrate drastically different behaviours. The energy required for the flow of blade has been reduced to almost zero for powder A even at a low air velocity of 1 mm/s and remained near zero for the higher velocities (2 – 5 mm/s) as well. As for the powder B, the zero plateau was never achieved even with an air velocity as high as 150 mm/s. The zero energy indicates a virtually fluidized powder bed that makes the rotation of the blade through the powder bulk easier. The sharp decrease in the amount of energy for the hybrid powder and reaching the fluidization state confirms the non-cohesive behavior of powder A.

17

The compressibility and permeability test results are shown in Figure 8.d and Figure 8.e, respectively. In these two tests a sample of pre-conditioned powder is compressed under certain normal stress values. The compressibility test measures the change in the powder volume when exposed to normal stress, and the permeation quantifies the ability of the bulk powder in passing a fluid through its porous structure by measuring the air pressure needed in order to maintain a constant air flow as the normal stress is increased. Figure 8.d shows that powder B is 4 – 6 times more compressible than powder A at any given normal stress. Powders with lower compressibility have a more efficient packing of particles, and are less cohesive. On the other hand, the pressure drop for powder A is approximately 10 mBar more than that of the powder B which makes the hybrid powder highly permeable to air.

The shear strength was measured at 7, 6, 5, 4, and 3 KPa normal stresses after pre-shearing the powder at 9 KPa. The higher value of shear stress at any given normal stress indicates a more difficult flow due to cohesiveness, irregular shape of particles, void-free structure etc. Powder A demonstrates lower shear yield loci for any normal stress compared to powder B making it less resistant to the flow during the recoating process. The results of powder morphology and rheology tests are indicative of the superiority of powder A for use in PBBJ process. This powder has been used throughout the rest of study for fabrication of samples for shape fidelity, tomography, and durometry experiments.

3.5 Part Shape Fidelity Characterization

The significance of layer thickness (LT) and silicone binder deposition frequency (Fr) on the dimensional accuracy of the 3D printed parts was evaluated using a multi-level experimental design. The details of design and the measured values for height and width can be found in Data

in Brief, Table 1. The samples were manufactured in a completely randomized order according to the designed experiment. The responses were assumed to be independent.

The analysis of variance (ANOVA) results are shown in Data in Brief Tables 2, 3, and 4 for H, ID, and DD, respectively. The results show that for H and ID, Fr has a significant effect at 95% confidence level. However, none of the parameters are significant at 95% confidence level for the DD. The response surface plots (Figure 9.a(i) - c(i)) demonstrate the path to the optimization for each of the responses. Marginal mean plots (Figure 9..a(ii) - c(ii)) confirm the ANOVA conclusions. The marginal mean plots for H and ID both show that the higher limit of LT (100 µm) yields dimensional values closer to the target. However, Fr of 1 drop per 200 µm and 1 drop per 300 µm produce the best results for H and ID, respectively. Thus, the desirability function technique was adopted to optimize the input parameters simultaneously (Data in Brief, Table 5). The simultaneous optimization of three responses showed that by setting LT and Fr both at their high level (100 µm and 1 drop per 300 µm respectively), the optimum results will be achieved. At this condition, the average values of ID, H, and DD will be 5.45 mm, 3.77 mm, and 1.6 mm respectively.

3.6   Part Internal Features

The CT scanning results at 4.05 voxel resolution for the entire AM-made silicone structure manufactured using 100 µm LT and 1 droplet per 3 layers Fr is shown in Figure 10.a. A higher concentration of silicone powder is visible in the center of the structure as opposed to its shell. The quantified vertical and radial particle phase fraction for each slice are plotted in Figure 11.a and Figure 11.b respectively, and demonstrate that the particle phase fraction is dropped from 75% at core to 55% at the edge. This change in the density of powder however is less variant along the

19

height of the sample (55% - 65%). A magnified view of two regions of interest inside the structure at higher resolution helps in distinguishing between the particle and cured binder phases. Figure.10.b shows a zone inside the structure with visibly higher concentration of silicone powder particles. Comparing these images with the CT scan results of a central section of the structure (Figure 10.c) reveals that the difference in concentration of particles is much higher in radial direction. The overall solid particle phase density for this cylindrical structure is 59.8%. The remaining 40.2% of the entire volume is comprised of silicone binder and pores.

In order to separate the silicone binder and air pores, image processing was conducted on the CT scanning data obtained for a small section of the AM-made part at nano-resolution (727 nm voxel resolution). Figure 12.a shows the overall view of the scanned samples. Silicone binder and pores are isolated in Figure 12.b and Figure 12.c, respectively. Based on the quantification results of image processing, the sample is made of 70.5% silicone powder, 21.3% silicone binder, and 8.2% pore. Five of the largest pores are shown in different colors in Figure 12.d. The distribution of pore network throughout the entire structure can also be found in video 1 of supporting information.

3.7 Part Durometry

Two sets of parts were 3D printed at optimized printing conditions (LT of 100 µm and Fr 1 drop per 300 µm). Three cylindrical parts from each batch were selected for the hardness test. The tests were replicated three times for each part. Similar testing approach was employed for the cured silicone binder molded based on ASTM D2240. The hardness test results are summarized inTable.4.. The ANOVA study was used to compare the average hardness of AM-made cylinders,

20

the results of which (Table 4.) failed to show a significant difference between the hardness of the parts. The hardness of parts printed at non-optimum conditions are provided in Tables 6 – 10 of Data in Brief. The average hardness values compared in Figure 3 of Data in Brief show a positive shift of ~ 8 (Shore 00) in the hardness when the layer thickness is increased to 100 μm. No systematic change in the average value of the hardness can be attributed to the dispensing frequency.

Similarly, the comparison of average hardness values for the AM-made cylinders and the pure silicone binder using a t-test does not show a statistically significant difference at 95% confidence level. The average hardness is approximately 83.6 (shore A) for the 3D printed parts and 79.8 (shore A) for the crosslinked silicone binder. The hardness of powder A, reported in the material's certificate, is 70 (shore A).

4   Discussion

The constant diameter of silicone binder droplet before separation from the needle tip under different pressure values (1.54 mm) allows the adjusting of the dispensing time by modifying the air pressure (Figure 4.a). The viscosity of silicone binder (78 mPa.s) is not very high so that it prevents the creation and separation of droplets, at the same time, it is not very low to cause fluid dripping (Figure 4.b). However, once dispensed on the dry powder bed, the infiltration process takes 10 – 20 s. Moreover, this long infiltration causes the disturbance of silicone powder particle distribution in the layer. In order to minimize this issue, the powder surface was pre-wetted with the water-based binder. The utilization of the water-based binder helps the proposed hybrid AM technique by: (i) binding the silicone particles temporarily together; (ii) speeding up the process of silicone binder infiltration to less than 1 s by enhancing the wetting properties of silicone

21

particles. The aqueous binder is used to wet the powder substrate in order to accelerate the progression of the silicone liquid droplet from primary to secondary liquid spread [61]. Primary spread occurs when the sessile droplet volume (volume above the powder) is not zero, where the secondary spread occurs within the porous substrate only. In the absence of the aqueous binder, the primary spread could take more than 10s, while in the presence of the aqueous binder, the primary spread is reduced to approximately 1s. The difference in the timing of infiltration of silicone binder on the dry and wet surfaces is shown in video 2 of the supporting information.

Investigating the thermal behaviour of the curing process of the liquid silicone binder is crucial in designing a curing mechanism that assures the geometrical accuracy of the parts is maintained by crosslinking the silicone binder after dispensing as fast as possible to prevent its penetration into the surrounding powder environment. The entire curing process for silicone binder at 90 $^{\circ}$C takes approximately 6 min which can prolong the manufacturing process. As a result, the silicone binder was exposed to a curing temperature between $100 - 120\,^{\circ}$C for 60 s using a thermal lamp. The changes in the powder surface temperature measured using a thermocouple (Data in Brief Figure 1) shows that the powder bed temperature reaches 100 $^{\circ}$C after 50 s and 110 $^{\circ}$C after 60 s. The isothermal plots at these two temperatures (Figure 5.c-d) demonstrate that curing happens immediately after reaching 100 $^{\circ}$C, and a full cure takes less than 1 min. As a result, the employed curing policy of 1 min exposure to heat prevents both the unnecessary increase in the total manufacturing time and permeation of silicone binder outside the region of interest.

When considering the liquid silicone material and the rheological and thermal behaviour during curing, it is recommended that for manufacturing of such silicone structures, the following considerations should be met: (i) increasing the infiltration rate of liquid silicone binder by enhancing its wettability through pre-wetting of powder-bed (ii) preventing the permeation of

22

silicone binder to the areas that are not supposed to be a part of final structure through instant curing (iii) tailoring the rheological properties of silicone binder (recommended viscosity range: 70 – 90 mPa.s) so that it not too viscous for common direct write AM techniques, yet viscous enough so that it does not permeate too fast before crosslinking, (iv) increasing the resolution and accuracy of the technique by replacing the extrusion system with a drop-on-demand AM printhead in order to reduce the diameter of silicone binder droplets to less than 300 µm.

The deep understanding the powder rheology and properties is important in powder-bed AM processes in order to obtain a consistent and uniformly spread layer and minimize the printing variability. Thus, investigating the rheological properties of a silicone powder with successful flowability for AM would be beneficial for future development of silicone powder customized for powder bed systems. Comparison of the shape and size of powders A and B (Figure 6) suggests that powder A could be a viable candidate for powder bed AM. Powders A and B both have a narrow particle size distribution range and spherical shape which are both favourable powder characteristics for AM. However, the smaller particle size of powder B (almost half the size of powder A) increases the free surface area and consequently the friction and static forces between the powder particles. This will result in the inefficient packing properties and difficulty in the powder spreading and layer recoating process [62]. The lower flowability under static and aerated conditions, lower permeability, and higher compressibility of powder B confirm the conclusions inferred from particle shape and size analyses. A high degree of agglomeration was observed in the SEM image of powder B (Figure 6b). The reason behind the low flowability and permeability of silicone B could be the formation of tightly packed structures as finer separated silicone particles interlock through static can friction to form powder agglomerations. The high compressibility is an indicator of the cohesiveness of powder B which justifies the agglomeration. An important

23

characteristic of the powder feedstock used in AM is their shear stress as the particles slide relative to each other when transferred from the feeding compartment to the building compartment by the roller, and the initiation of the flow is dependent on overcoming the resistance to the flow. The lower shear stress for the powder A shows its better flow properties and less cohesive behavior. The lubricating effect derived from the resin coated hybrid powder A also contributes to its overcoming of the inter-particular shear forces.

When considering the powder silicone material and the rheological and morphology of the powders, it is recommended that for manufacturing of such silicone structures, the following considerations should be met: (i) spherical and symmetric powder particles; (ii) average particle size between $30 – 40$ µm with a reasonably wide distribution range (± 30 µm) to provide a efficient particle packing in the powder-bed; (iii) non-cohesive powder demonstrating limited compressibility ($10 – 20$ %) and high permeability to air; (iv) powder with low shear yield (less than 2.5 KPa for normal pressure between $1 – 7$ KPa) to decrease the resistance to flow during the recoating.

The investigation of part shape fidelity through the experimental design showed that at the optimum condition, the H and ID of the sample parts are 0.45 mm and 0.75 mm larger than their target values, respectively. Moreover, the optimized DD value of 1.7 mm will reduce the geometrical accuracy of the shape. The results show that further work in this area must be done in order to obtain higher geometrical accuracy. To this end, the effect of surfactants on the surface properties and the size of silicone binder droplet and the effect of additives to the powder system for controlling its fluid permeability properties will be investigated in the future work.

Based on the CT scan data, the silicone part fabricated at optimum printing condition using the hybrid method consists of approximately 8.2% air voids (Figure 12) which are distributed unevenly throughout the structure (Figure 11). Moreover, despite the presence of regional pore interconnectivity at multiple locations in the AM-made sample (video 1), the pores of larger volume are actually isolated and trapped inside the part (Figure 12d). As a result, a new dispensing method using piezo-dispensing should be investigated to determine the feasibility of dispensing smaller liquid silicone droplet volumes throughout the layer of interest to increase shape fidelity and control over the internal porosity. Printing droplets with volumes in the order of pico- or micro-liter provides higher control and flexibility over the total silicone binder volume infiltrated in each layer, and makes it possible to fill a certain percentage of the air voids. In such drop-on-demand systems, adjusting the actuation parameters in combination with translational velocity of the printhead can change the volume of droplets as well as the deposition frequency. Thus, multiple patterns from continuous lines to separate droplets can be laid down on the powder substrate which in turn make controlling the overall density of the structure possible. This provides an apparatus for fabrication of silicone structures with variable density profile from fully dense to highly porous with interconnected channels.

The CT analysis results illustrated in Figure 11.showed a variability in silicone powder volume fraction radially, with more particles clustering in the center compared to the periphery of the parts. This is an artefact of the droplet deposition process. When infiltrating polymer solution droplets onto a porous substrate [63], the liquid permeation through the porous powder media is dependent on the droplet kinetics, porosity of the substrate, as well as the wetting angle of the powder material. Considering that the size of the liquid silicone droplet (approximately 1.54 mm) is significantly larger than the average powder particle size used in this study (powder Type A, 30

25

µm), the dynamic impact kinetics of the traveling droplet and liquid spreading mechanisms of the sessile droplet through the porous media can play a significant role in disturbing the powder [61]. The impact kinetics of the falling droplet can explain the regions of higher powder particle concentration at the bottom of the parts, as particles are displaced vertically [63]. The difference in powder fraction radially, from 75% volume fraction of particles in the centre of the part to 55% at the periphery, can be explained by the theory of droplet primary and secondary liquid spread [61]. In the primary spread, the liquid droplet meets the substrate and starts to imbibe the powder. During this phase, there is an instantaneous flow rate initiated at the liquid-powder interface. This generates a net force acting at the inlet powder boundary, thus particles can be dislodged and can travel within the sessile droplet radially, which may explain the different concentration of particles in the centre of the parts. Overall, the theory seems to suggest that smaller liquid silicone droplets would reduce the powder displacement and likely result in a more uniform component, furthering the need for a better liquid silicone delivery method.

The durometry results for the AM-made samples show that different replicates of the same manufacturing process produce similar durometry results which indicate the reproducibility of the hybrid PBBJ-extrusion process. Moreover, the hardness of these composite parts made with different printing parameters is between 70 – 80 (Shore A), so are the hardness of silicone binder and powder. No clear relationship between the printing parameters and the hardness was established at this time. A full mechanical characterization will be carried out on the products of this AM method in the future. Specifically, the effect of the printing parameters on the tensile strength, tear strength, and elongation at break of the parts [64] should be investigated in order to make any required changes to the system of materials for each particular biomedical application.

This study showcased the possibility of manufacturing silicone structures using a hybrid powder bed binder jetting and liquid dispensing process, which offers new opportunities to locally tailor the material porosity and intrinsically mechanical properties. The experimental results indicated that PBBJ technique is capable of processing thermoset powders. The main challenge remaining is integration of a multi-nozzle inkjet printhead compatible with medium to high viscous silicone binders to the system. Such a binder deposition system will increase the AM speed, improves the geometrical accuracy of the final products, and provides higher control over the properties of parts. Upon further improvement in the deposition of silicone binder, this hybrid method could be used for production of structures with the capability of controlled release of fluids for drug-delivery applications.

5   Conclusion

In this research work, a novel hybrid method combining PBBJ and deposition techniques for fabrication of 3D structures entirely made from silicone was introduced. Cylindrical samples optimized in terms of geometrical accuracy were showcased. The permeation of silicone binder in the powder bed was sped up by pre-wetting the surface with an aqueous binder. The rapid curing mechanism of the parts was designed based on the thermal analysis of the binder. Guidelines for efficient flowability of silicone powder were provided based on its rheological properties and shear sensitivity. The results of this work show the potential of binder jetting AM techniques in fabrication of complex, customized, and intelligent structures for application in pharmaceutical, biomedical, and life sciences.

Acknowledgments

28

References

[1] D.F. Butler, G.G. Gion, R.P. Rapini, Silicone auricular prosthesis, J. Am. Acad. Dermatol. 43 (2000) 687-690.

[2] E. In, E. Walker, H. Naguib, Novel Development of 3D printable UV-curable Silicone for Multimodal Imaging Phantom (2017).

[3] R. Schüler, M. Wittkampf, G. Chemnitius, Modified gas-permeable silicone rubber membranes for covalent immobilisation of enzymes and their use in biosensor development, Analyst 124 (1999) 1181-1184.

[4] J. Ren, L. Wang, X. Han, J. Cheng, H. Lv, J. Wang, X. Jian, M. Zhao, L. Jia, Organic Silicone Sol–Gel Polymer as a Noncovalent Carrier of Receptor Proteins for Label-Free Optical Biosensor Application 5 (2012) 386-394.

[5] G. Golomb, M. Dixon, M.S. Smith, F.J. Schoen, R.J. Levy, Controlled- release drug delivery of diphosphonates to inhibit bioprosthetic heart valve calcification: Release rate modulation with silicone matrices via drug solubility and membrane coating, J. Pharm. Sci. 76 (1987) 271-276.

[6] W. Noll, Chemistry and technology of silicones, Elsevier, 2012.

[7] A.K. Au, W. Lee, A. Folch, Mail-order microfluidics: evaluation of stereolithography for the production of microfluidic devices 14 (2014) 1294-1301.

[8] J. Rossiter, P. Walters, B. Stoimenov, Printing 3D dielectric elastomer actuators for soft robotics (2009) 72870H-72870H-10.

[9] A. Creegan, I. Anderson, 3d printing for dielectric elastomers (2014) 905629-905629-10.

[10] N.H. Cohrs, A. Petrou, M. Loepfe, M. Yliruka, C.M. Schumacher, A.X. Kohll, C.T. Starck, M. Schmid Daners, M. Meboldt, V. Falk, A Soft Total Artificial Heart—First Concept Evaluation on a Hybrid Mock Circulation, Artif. Organs (2017).

[11] K. Xiao, F. Zardawi, R. van Noort, J.M. Yates, Developing a 3D colour image reproduction system for additive manufacturing of facial prostheses 70 (2014) 2043-2049.

[12] F.M. Zardawi, K. Xiao, R. Van Noort, J.M. Yates, Investigation of Elastomer Infiltration into 3D Printed Facial Soft Tissue Prostheses 4 (2015) 2161-1173.

[13] D. Eggbeer, R. Bibb, P. Evans, L. Ji, Evaluation of direct and indirect additive manufacture of maxillofacial prostheses, Proc. Inst. Mech. Eng. H. 226 (2012) 718-728.

[14] R. Bibb, D. Eggbeer, P. Evans, Rapid prototyping technologies in soft tissue facial prosthetics: current state of the art 16 (2010) 130-137.

[15] S. Bai, Z. Feng, R. Gao, Y. Dong, Y. Bi, G. Wu, X. Chen, Development and application of a rapid rehabilitation system for reconstruction of maxillofacial soft-tissue defects related to war and traumatic injuries 1 (2014) 11.

[16] T. Kojima, Salivary Gland Development and Regeneration, in: Anonymous , Regenerative Medicine in Otolaryngology, Springer, 2015, pp. 209-223.

[17] M.S. Mannoor, Z. Jiang, T. James, Y.L. Kong, K.A. Malatesta, W.O. Soboyejo, N. Verma, D.H. Gracias, M.C. McAlpine, 3D printed bionic ears 13 (2013) 2634-2639.

[18] E.B. Duoss, T.H. Weisgraber, K. Hearon, C. Zhu, W. Small, T.R. Metz, J.J. Vericella, H.D. Barth, J.D. Kuntz, R.S. Maxwell, Three- dimensional printing of elastomeric, cellular architectures with negative stiffness 24 (2014) 4905-4913.

[19] F. Liravi, R. Darleux, E. Toyserkani, Nozzle dispensing additive manufacturing of polysiloxane: dimensional control 5 (2015) 20-43.

[20] D.B. Kolesky, R.L. Truby, A. Gladman, T.A. Busbee, K.A. Homan, J.A. Lewis, 3D bioprinting of vascularized, heterogeneous cell- laden tissue constructs, Adv Mater 26 (2014) 3124-3130.

[21] D.B. Kolesky, K.A. Homan, M.A. Skylar-Scott, J.A. Lewis, Three-dimensional bioprinting of thick vascularized tissues, Proc. Natl. Acad. Sci. U. S. A. 113 (2016) 3179-3184.

[22] K. Tian, J. Bae, S.E. Bakarich, C. Yang, R.D. Gately, G.M. Spinks, Z. Suo, J.J. Vlassak, 3D Printing of Transparent and Conductive Heterogeneous Hydrogel–Elastomer Systems, Adv Mater (2017).

[23] A.M. Schmalzer, C.M. Cady, D. Geller, D. Ortiz-Acosta, A.T. Zocco, J. Stull, A. Labouriau, Gamma radiation effects on siloxane-based additive manufactured structures, Radiat. Phys. Chem. 130 (2017) 103-111.

[24] S.V. Murphy, A. Atala, 3D bioprinting of tissues and organs, Nat. Biotechnol. 32 (2014) 773-785.

[25] C.C. Chang, E.D. Boland, S.K. Williams, J.B. Hoying, Direct- write bioprinting three-dimensional biohybrid systems for future regenerative therapies 98 (2011) 160-170.

[26] T.J. Hinton, A.R. Hudson, K. Pusch, A. Lee, A.W. Feinberg, 3D Printing PDMS Elastomer in a Hydrophilic Support Bath via Freeform Reversible Embedding 2 (2016) 1781-1786.

[27] C.S. O'Bryan, T. Bhattacharjee, S. Hart, C.P. Kabb, K.D. Schulze, I. Chilakala, B.S. Sumerlin, W.G. Sawyer, T.E. Angelini, Self-assembled micro-organogels for 3D printing silicone structures 3 (2017) e1602800.

[28] T. Fripp, N. Frewer, L. Green (2014).

[29] D.S.D. Kim, B.L. Tai, Hydrostatic support-free fabrication of three-dimensional soft structures 24 (2016) 391-396.

[30] D.S.D. Kim, S. Thompson, M. Grunlan, B.L. Tai, Optimization of Low One-photon Polymerization for Hydrostatic 3D Printing of Silicone Material.

[31] F.P. Melchels, J. Feijen, D.W. Grijpma, A review on stereolithography and its applications in biomedical engineering, Biomaterials 31 (2010) 6121-6130.

[32] E. Selbertinger, F. Achenbach, B. Pachaly (2015).

[33] S. Reitelshöfer, M. Göttler, P. Schmidt, P. Treffer, M. Landgraf, J. Franke, Aerosol-Jet-Printing silicone layers and electrodes for stacked dielectric elastomer actuators in one processing device 9798 (2016) 97981Y-97981Y-9.

[34] I. Gibson, D.W. Rosen, B. Stucker, Additive manufacturing technologies, Springer, 2010.

[35] F. Liravi, E. Toyserkani, A hybrid additive manufacturing method for the fabrication of silicone bio-structures: 3D printing optimization and surface characterization, Mater Des 138 (2017) 46-61.

[36] E.M. Sachs, J.S. Haggerty, M.J. Cima, P.A. Williams (1993).

[37] D. Bourell, J.P. Kruth, M. Leu, G. Levy, D. Rosen, A.M. Beese, A. Clare, Materials for additive manufacturing (2017).

[38] S.B. Hong, N. Eliaz, G.G. Leisk, E.M. Sach, R.M. Latanision, S.M. Allen, A new Ti-5Ag alloy for customized prostheses by three-dimensional printing (3DP), J. Dent. Res. 80 (2001) 860-863.

[39] Y. Shanjani, Y. Hu, R.M. Pilliar, E. Toyserkani, Mechanical characteristics of solid-freeform-fabricated porous calcium polyphosphate structures with oriented stacked layers 7 (2011) 1788-1796.

[40] P. Habibovic, U. Gbureck, C.J. Doillon, D.C. Bassett, C.A. van Blitterswijk, J.E. Barralet, Osteoconduction and osteoinduction of low-temperature 3D printed bioceramic implants, Biomaterials 29 (2008) 944-953.

[41] U. Gbureck, E. Vorndran, F.A. Müller, J.E. Barralet, Low temperature direct 3D printed bioceramics and biocomposites as drug release matrices, J. Controlled Release 122 (2007) 173-180.

[42] A. Khalyfa, S. Vogt, J. Weisser, G. Grimm, A. Rechtenbach, W. Meyer, M. Schnabelrauch, Development of a new calcium phosphate powder-binder system for the 3D printing of patient specific implants, J. Mater. Sci. Mater. Med. 18 (2007) 909-916.

[43] K. Igawa, M. Mochizuki, O. Sugimori, K. Shimizu, K. Yamazawa, H. Kawaguchi, K. Nakamura, T. Takato, R. Nishimura, S. Suzuki, Tailor-made tricalcium phosphate bone implant directly fabricated by a three-dimensional ink-jet printer 9 (2006) 234-240.

[44] A. Butscher, M. Bohner, S. Hofmann, L. Gauckler, R. Müller, Structural and material approaches to bone tissue engineering in powder-based three-dimensional printing 7 (2011) 907-920.

[45] B. Stevens, Y. Yang, A. Mohandas, B. Stucker, K.T. Nguyen, A review of materials, fabrication methods, and strategies used to enhance bone regeneration in engineered bone tissues 85 (2008) 573-582.

[46] M. Castilho, I. Pires, B. Gouveia, J. Rodrigues, Structural evaluation of scaffolds prototypes produced by three-dimensional printing 56 (2011) 561-569.

[47] S. Yang, K. Leong, Z. Du, C. Chua, The design of scaffolds for use in tissue engineering. Part II. Rapid prototyping techniques, Tissue Eng. 8 (2002) 1-11.

[48] M. Vlasea, E. Toyserkani, R. Pilliar, Effect of gray scale binder levels on additive manufacturing of porous scaffolds with heterogeneous properties 12 (2015) 62-70.

[49] D.W. Hutmacher, M. Sittinger, M.V. Risbud, Scaffold-based tissue engineering: rationale for computer-aided design and solid free-form fabrication systems, Trends Biotechnol. 22 (2004) 354-362.

[50] D.W. Hutmacher, Scaffolds in tissue engineering bone and cartilage, Biomaterials 21 (2000) 2529-2543.

[51] M. Castilho, M. Dias, U. Gbureck, J. Groll, P. Fernandes, I. Pires, B. Gouveia, J. Rodrigues, E. Vorndran, Fabrication of computationally designed scaffolds by low temperature 3D printing 5 (2013) 035012.

[52] P.H. Warnke, H. Seitz, F. Warnke, S.T. Becker, S. Sivananthan, E. Sherry, Q. Liu, J. Wiltfang, T. Douglas, Ceramic scaffolds produced by computer-assisted 3D printing and sintering: Characterization and biocompatibility investigations 93 (2010) 212-217.

[53] F.M. Zardawi, Characterisation of Implant Supported Soft Tissue Prostheses Produced with 3D Colour Printing Technology (2013).

[54] S. Yang, K. Leong, Z. Du, C. Chua, The design of scaffolds for use in tissue engineering. Part I. Traditional factors, Tissue Eng. 7 (2001) 679-689.

[55] K. Leong, C. Cheah, C. Chua, Solid freeform fabrication of three-dimensional scaffolds for engineering replacement tissues and organs, Biomaterials 24 (2003) 2363-2378.

[56] W. Chiu, K. Yu, Direct digital manufacturing of three-dimensional functionally graded material objects, Comput. -Aided Des. 40 (2008) 1080-1093.

[57] M. Vlasea, E. Toyserkani, Experimental characterization and numerical modeling of a micro-syringe deposition system for dispensing sacrificial photopolymers on particulate ceramic substrates, J. Mater. Process. Technol. 213 (2013) 1970-1977.

[58] R. Freeman, X. Fu, Characterisation of powder bulk, dynamic flow and shear properties in relation to die filling 51 (2008) 196-201.

[59] X. Fu, D. Huck, L. Makein, B. Armstrong, U. Willen, T. Freeman, Effect of particle shape and size on flow properties of lactose powders 10 (2012) 203-208.

[60] R. Freeman, Measuring the flow properties of consolidated, conditioned and aerated powders—a comparative study using a powder rheometer and a rotational shear cell, Powder Technol 174 (2007) 25-33.

[61] B. Markicevic, T. D'Onofrio, H. Navaz, On spread extent of sessile droplet into porous medium: Numerical solution and comparisons with experiments, Phys. Fluids 22 (2010) 012103.

[62] S. Hatami, O. Lyckfeldt, L. Tönnäng, K. Fransson, Flow properties of tool steel powders for selective laser melting–influence of thermal and mechanical powder treatments 60 (2017) 353-362.

[63] R.K. Holman, M.J. Cima, S.A. Uhland, E. Sachs, Spreading and infiltration of inkjet-printed polymer solution droplets on a porous substrate, J. Colloid Interface Sci. 249 (2002) 432-440.

[64] T. Aziz, M. Waters, R. Jagger, Analysis of the properties of silicone rubber maxillofacial prosthetic materials, J. Dent. 31 (2003) 67-74.
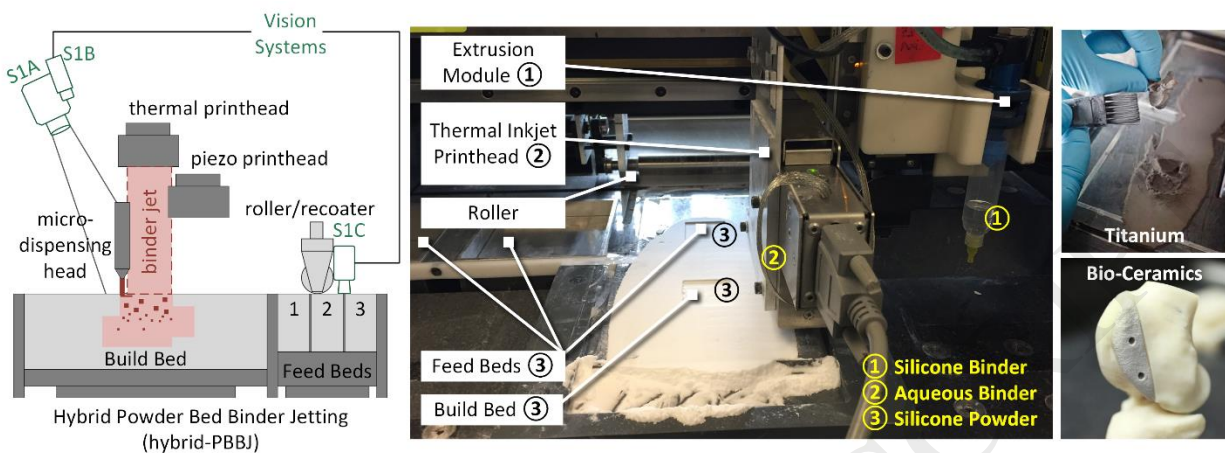
Figures:

Figure 1 The hybrid PBBJ AM system schematic (left) and physical system showcasing the multi-powder material feedstock capabilities, micro-dispensing syringe system, as well as examples of calcium polyphosphate bioceramic and commercially pure titanium parts manufactured using the system (right).
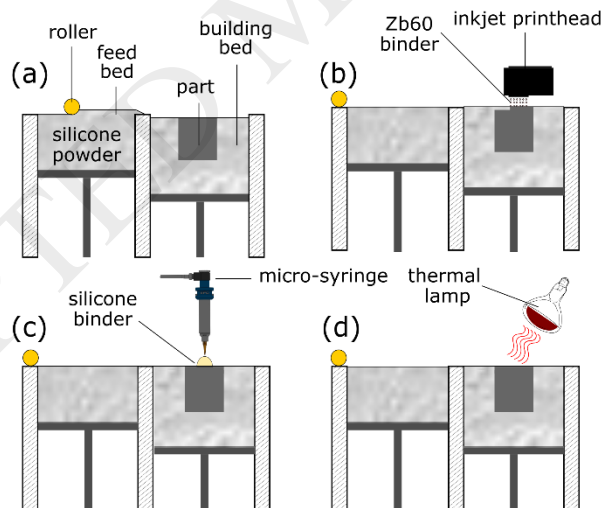

Figure 2 The schematic of hybrid PBBJ AM system. (a) spreading the silicone powder from feed bed onto the build bed; (b) wetting each layer by inkjet printing the water-based binder; (c) dispensing a droplet of silicone binder to fill up the silicone porous media using a pneumatic extrusion system; (d) partial curing of the silicone binder using a thermal lamp at 100ºC temperature.
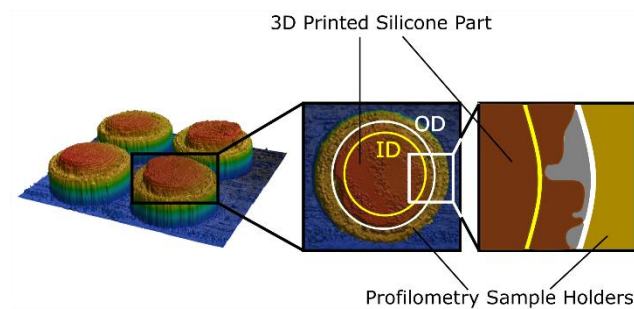
Figure 3 Sample of the 3D profile of the four replications of a part manufactured with similar printing parameters. The difference between the two circles fitted to the cross-section of each sample is shown in the magnified top view images.
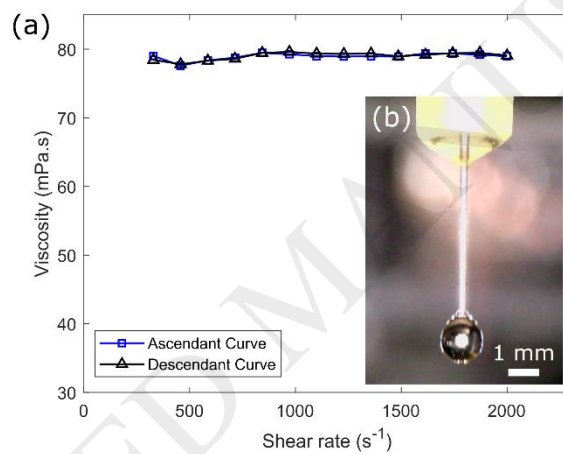

Figure 4 (a) The viscosity of silicone binder showing a Newtonian behavior at the shear rate range of 200 – 2000 s^{-1}; (b) The silicone binder droplet before separation from the needle with a maximum diameter of 1.54 mm
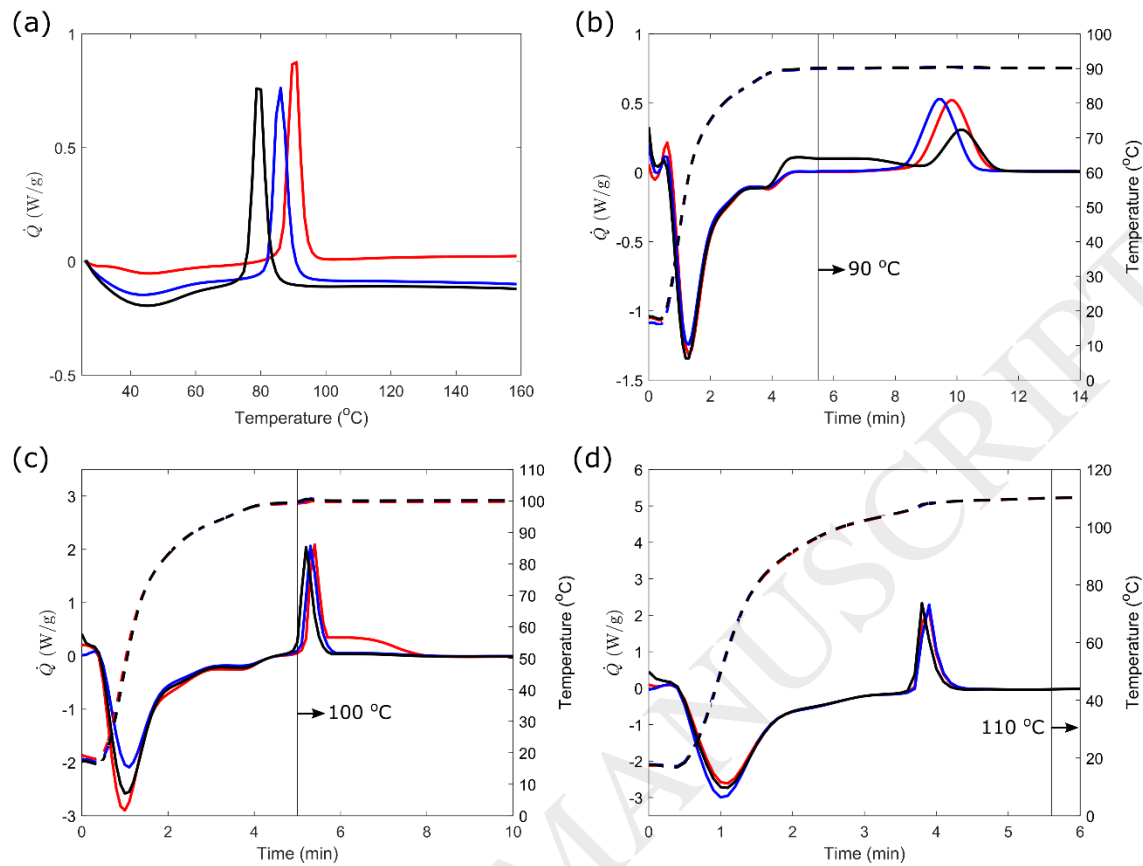
Figure 5 Thermal analysis results for silicone binder (100:1); (a) non-isothermal curves (heat flux vs. temperature) ; (b) isothermal curves at 90 ºC; (c) isothermal curves at 100 ºC; (d) isothermal curves at 110 ºC; (a-d) n=3, solid lines and dashed line corresponds to heat flux and temperature, respectively.
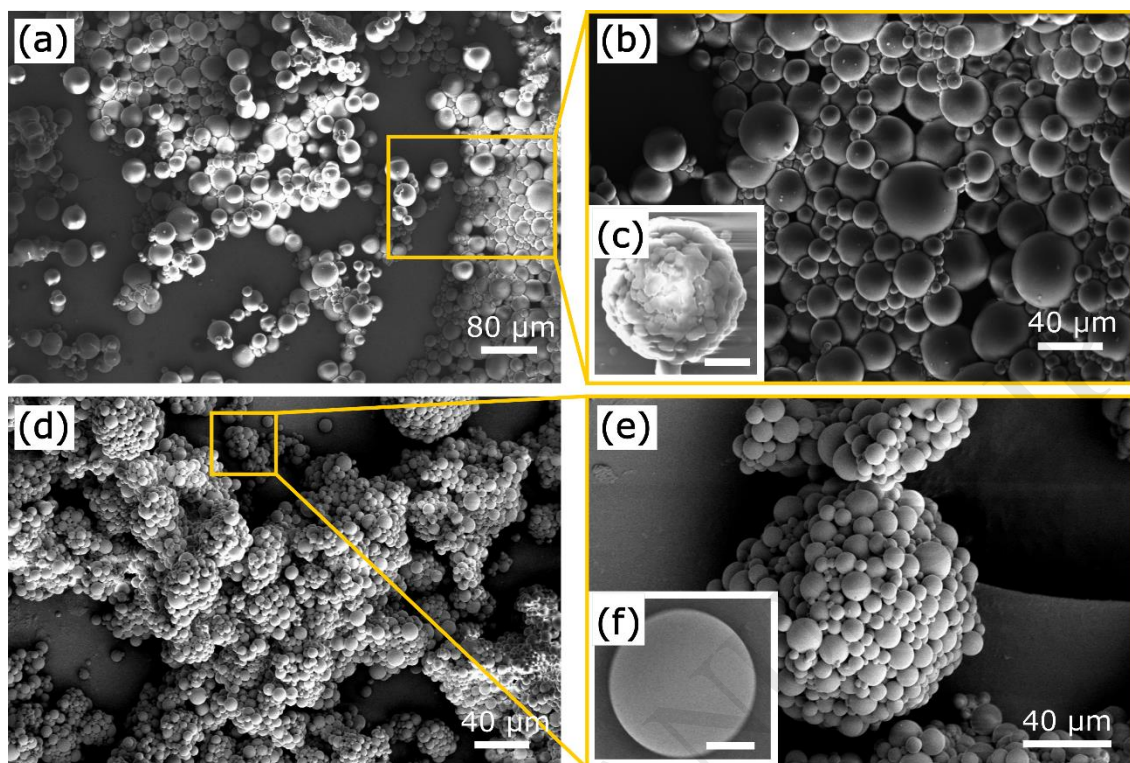
36

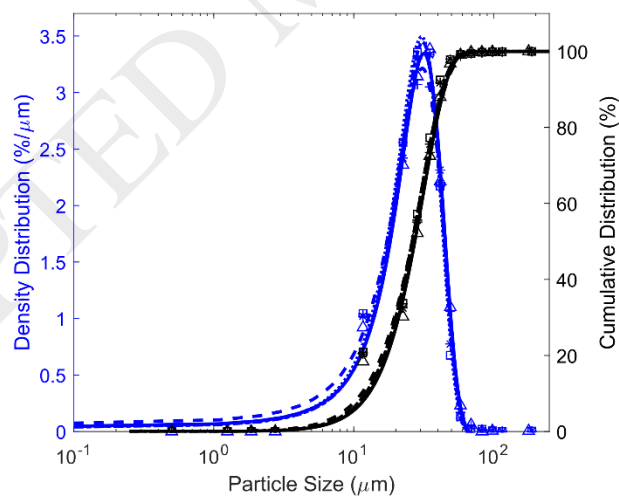Figure 6 (a-c) SEM images for powder A; (d-f) SEM images for powder B.

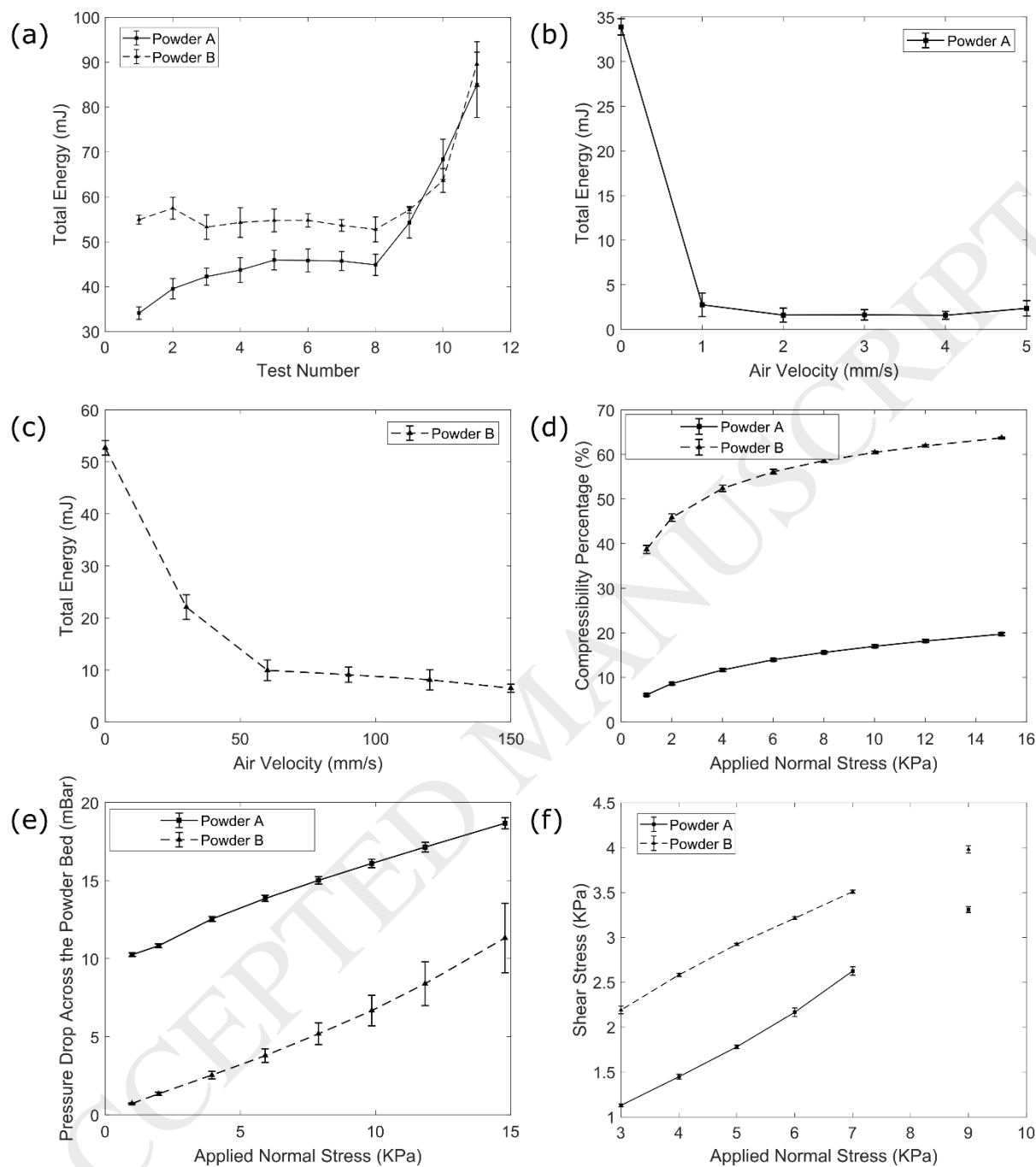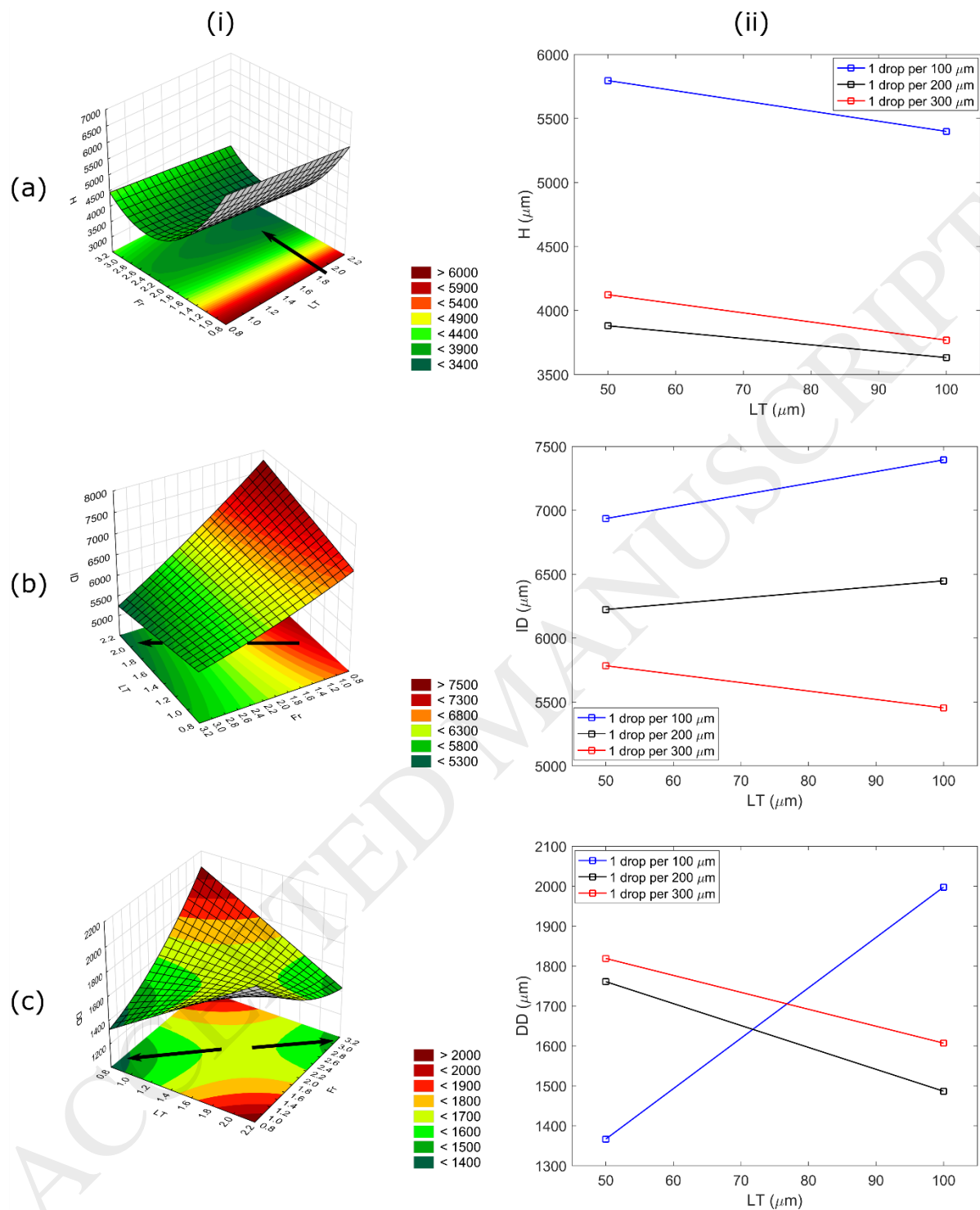Figure 7 Particle size distribution for powder A (n=3).

Figure 8 Silicone powder characterization results (n=3); (a) flow test for powders A and B; (b) aeration test for powder A; (c) aeration test for powder B; (d) compressibility results for powders A and B; (e) permeation results for powders A and B; (f) shearing test for powders A and B.

Figur 9 The optimization results for separate analysis of responses; (a-i) the contour plot and optimization path for H; (a-ii) the plot of marginal means for H; (b-i) the contour plot and optimization path for ID; (a-ii) the plot of marginal means for ID; (c-i) the contour plot and optimization path for DD; (c-ii) the plot of marginal means for DD.
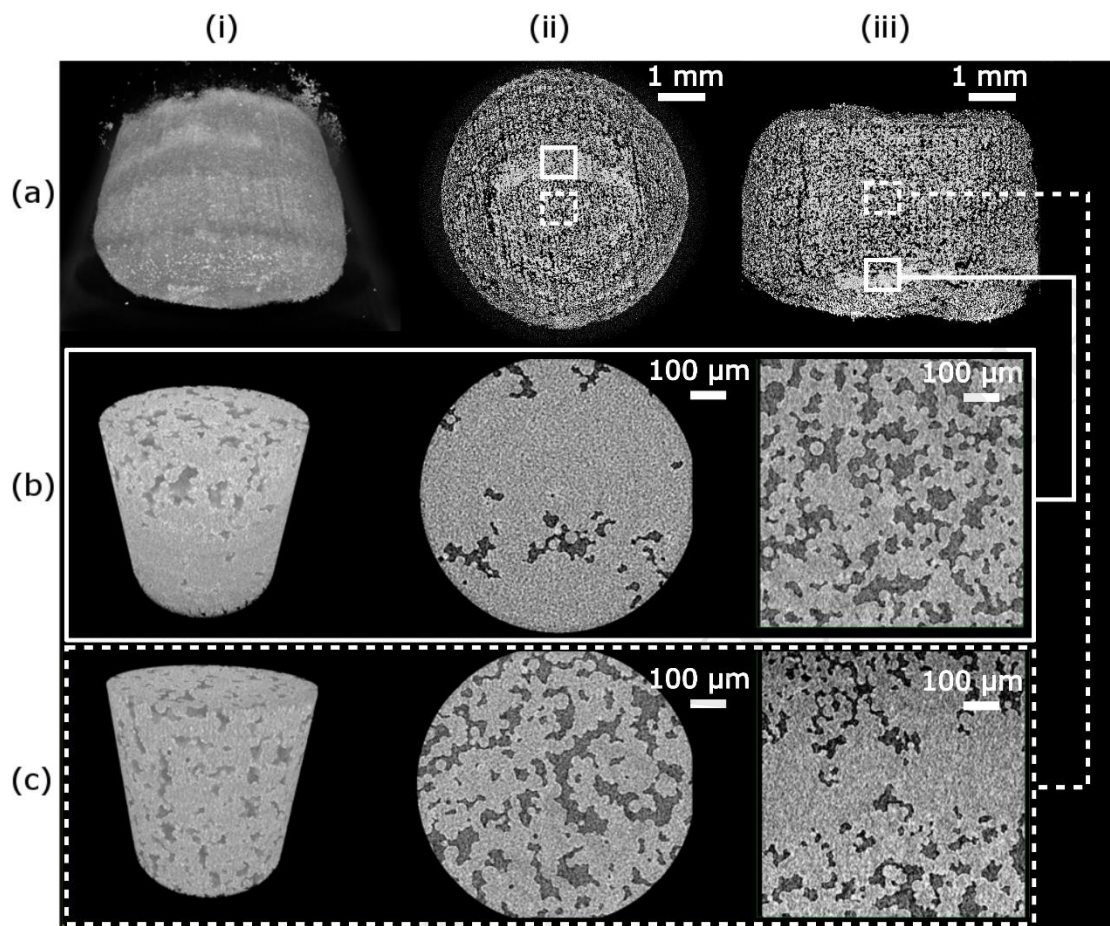
Figure 10 CT scanning results for the silicone part made via hybrid PBBJ-extrusion system; (a) overall structure, (b) defect region with high particle density; (c) central region with regular particle density; (a-c) (i) 3D view, (ii) top view, (iii) front view; (a) CT scanning resolution: 4.05 μm; (b-c) CT scanning resolution: 1.4 μm.
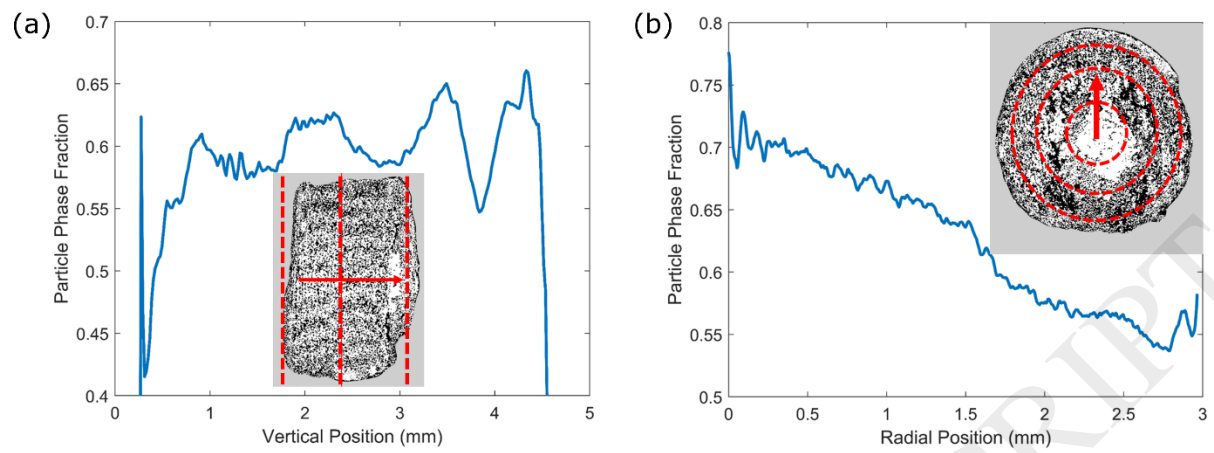
Figure 11 Silicone particle phase fraction vs. (a) vertical position and (b) radial position.
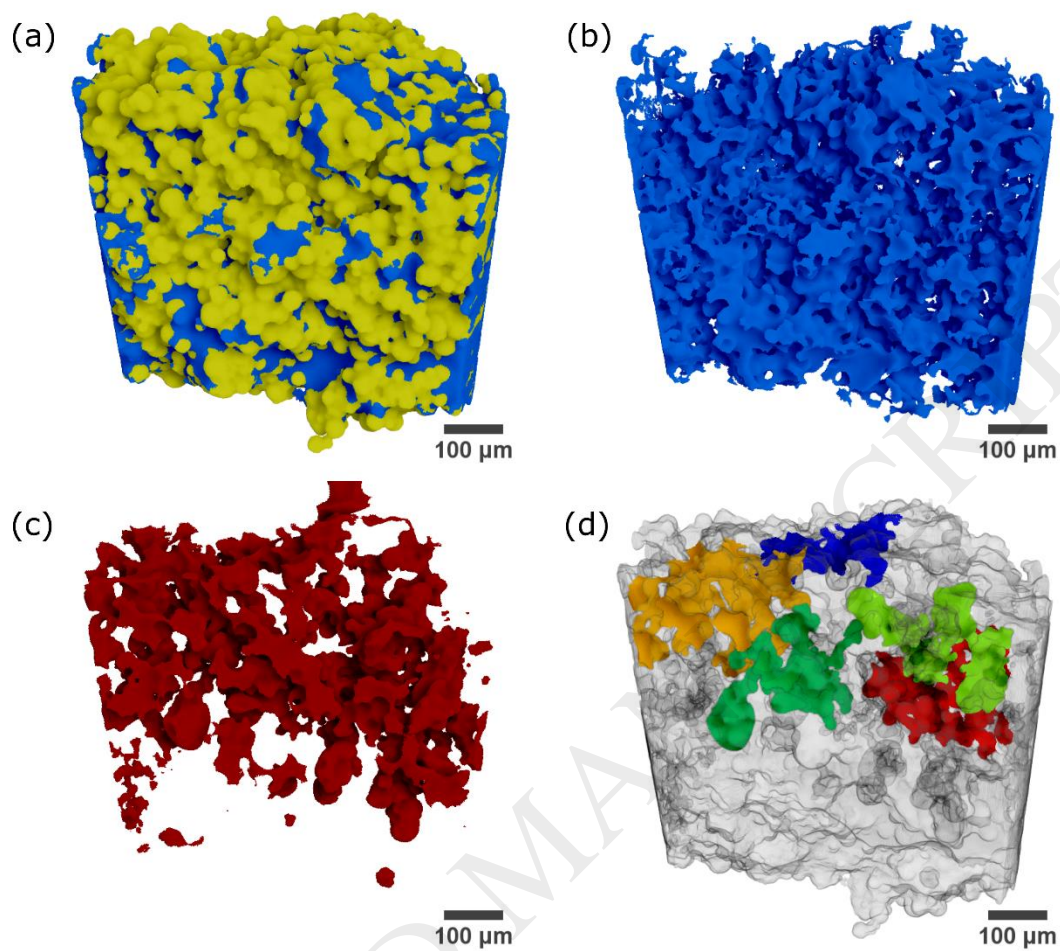
Figure 12 Separation of different phases of AM-made structure; (a) yellow: silicone powder, blue: cross-linked silicone binder; (b) isolated cross-linked silicone binder; (c) isolated pores; (d) largest air gaps in the pore network separated with different colors; (a-d) CT scanning resolution: 727 nm.

Tables:

Table 1 CT scanning parameters

Parameters	Voxel size (μm)		
	4.05	1.4	0.727
Source Power (W)	3	3	3
X-ray Energy (kV)	40	40	40
Filter	LE2	LE1	LE1
X-ray Optic Lens	4×	20×	20×
Exposure Time (s)	1	1	10
Number of Projections	801	801	1601
Binning Level	4	4	2

Table 2 Experimental design factor levels.

Factor	Low Level (-1)	Center Level (0)	High Level (+1)
LT - Layer Thickness (μm)	50	-	100
Fr - Dispensing Frequency	1 drop per 100 μm	1 drop per 200 μm	1 drop per 300 μm

Table 3 Dispensing duration for one droplet at different air pressure values.

Pressure (KPa)	Dispensing Time (s)
30	15
50	10
100	8

43

Table 4 The durometry results for the 3D printed cylinders and molded silicone binder (n=3).

Sample	Hardness (shore 00)			
	test 1	test 2	test 3	Avg.
Cylinder 1 (batch 1)	80.5	85.6	80.9	82.33
Cylinder 2 (batch 1)	87.3	85.2	82.8	85.10
Cylinder 3 (batch 1)	80.7	80.1	81.5	80.77
Cylinder 1 (batch 2)	81.5	85.3	86	84.27
Cylinder 2 (batch 2)	85.3	84.3	85.2	84.93
Cylinder 3 (batch 2)	80.9	87.8	84.7	84.47
Total Avg.				**83.64**
Molded silicone binder 1	81.5	80.1	75.4	79.00
Molded silicone binder 2	81.2	81.2	79.6	80.67
Total Avg.				**79.83**

Table 5 ANOVA results for the hardness test.

Source	DF	Adjusted Sum of Squares	Adjusted Mean Squares	F-Value	P-Value
Measurements	5	55.49	11.098	2.54	0.086
Error	12	52.47	4.373		
Total	17	107.96			

Table 6 T-test results for comparing the hardness of 3D printed structures and molded silicone binder.

	N	Mean	Standard Deviation	Standard Error Mean
3D printed parts	6	83.64	1.72	0.7
Molded binder	2	79.84	1.18	0.83

44